Titanium doped yttrium manganite: improvement of microstructural properties and peculiarities of multiferroic properties

Olivera Zemljak[a], Danijela Luković Golić[a*], Milica Počuča-Nešić[a], Aleksandra Dapčević[b], Pavla Šenjug[c], Damir Pajić[c], Tina Radošević[d], Goran Branković[a], Zorica Branković[a]

[a]University of Belgrade, Center of Excellence for Green Technologies - Institute for Multidisciplinary Research, Kneza Višeslava 1a, 11030 Belgrade, Serbia

[b]University of Belgrade, Faculty of Technology and Metallurgy, Karnegijeva 4, 11120 Belgrade, Serbia

[c]University of Zagreb, Department of Physics, Faculty of Science, Bijenička cesta 32, 10000 Zagreb, Croatia

[d] Jožef Stefan Institute, Department for Nanostructural Materials, Jamova cesta 39, 1000 Ljubljana, Slovenia

E-mail addresses of the authors: olivera.milosevic@imsi.bg.ac.rs; danijela@imsi.bg.ac.rs; milicaka@imsi.bg.ac.rs; hadzi-tonic@tmf.bg.ac.rs; psenjug@phy.hr; dpajic@phy.hr; tina.radosevic@ijs.si; goran.brankovic@imsi.bg.ac.rs; zorica.brankovic@imsi.bg.ac.rs

[*]**Corresponding author**: Danijela Luković Golić

University of Belgrade, Institute for Multidisciplinary Research, Department of Materials Science, Kneza Višeslava 1a, 11030 Belgrade, Serbia

E-mail: danijela@imsi.bg.ac.rs

Telephone number: (+381) 11 2085037

Fax number: (+381) 11 2085038

Abstract: Yttrium manganite, $YMnO_3$, was doped with different concentrations of titanium (x = 0, 0.04, 0.08, 0.10, 0.15, 0.20) in order to improve the microstructural and multiferroic properties. The powders were prepared using sol-gel polymerization complex method from citrate precursors. Depending on the titanium concentration, the hexagonal structure and/or the rhombohedral superstructure are present in the sintered samples. The $YMn_{1-x}Ti_xO_{3+\delta}$ (x = 0.10, 0.15, 0.20) ceramic samples showed significantly reduced density of microcracks, and of inter- and intragranular pores, and relative densities greater than 90 %. The structural parameters for $YMn_{1-x}Ti_xO_{3+\delta}$ (x = 0, 0.10, 0.15) were correlated with the results of magnetic and ferroelectric measurements. The most of titanium-doped samples showed a reduction of the leakage current density in comparison with undoped $YMnO_3$, and their ferroelectric responses were slightly improved. The modifications in structural arrangement resulted in partial suppression of ideal antiferromagnetic ordering visible through decrease of the Néel temperature and Weiss parameter, as well as the appearance of weak ferromagnetism and increase of magnetization (especially, in samples x = 0.08, 0.10, 0.15). These changes in physical quantities most likely originated from incorporation of the uncompensated magnetic moments and possible spin canting induced by enhanced symmetry break of the superexchange bridges.

Highlights

- Synthesis of $YMn_{1-x}Ti_xO_{3+\delta}$ (x = 0–0.20) powders using sol-gel polymerization complex method.
- Synthesis method and doping reduced microdefects and increased ceramics' relative density.
- The leakage currents decreased in $YMn_{1-x}Ti_xO_{3+\delta}$ ceramics upon doping.
- Reduction in geometrical frustration of antiferromagnetic structure after Ti-doping.
- Enhanced weak ferromagnetic response in $YMn_{1-x}Ti_xO_{3+\delta}$ (x = 0.10, 0.15, 0.08) samples.

Keywords: Ti-doped $YMnO_3$; sol-gel processing; ceramics; microcracks/micropores; ferroelectric properties; magnetic properties

1 Introduction

Multiferroic materials have been the subject of scientific research for many years because of their ability to simultaneously display two or more ferroic properties, such as (anti)ferromagnetism and ferroelectricity. Coupling between the electric polarization and magnetization allows control of magnetization by applying electric field and vice versa. It opens many possibilities for various technological applications, among which the most promising are in: sensors, spintronics, ferroelectric memory devices, microactuators, magnetic storage, piezoelectric sensors, among others [1–5].

Yttrium manganite ($YMnO_3$) belongs to the family of the rare-earth manganites, $RMnO_3$, where R represents rare-earth element. Yttrium manganese oxide displays multiferroic properties, simultaneously being ferroelectric and antiferromagnetic [1]. Hexagonal yttrium manganite (*h*-$YMnO_3$) has high ferroelectric Curie (T_C ~ 900 K) and low Néel temperature (T_N ~ 70 K) [6–10]. At room temperature, it exhibits non-centrosymmetric, polar structure (space group $P6_3cm$) [8], consisting of alternative layers of seven-coordinated Y^{3+} ions and corner-linked MnO_5 trigonal bipyramids [1, 9]. Tilting of the MnO_5 trigonal bipyramids towards the *ab* plane leads to displacement of the manganese ions from the centre of the bipyramid, causing the distortion of triangular lattice layers of Mn^{3+} in *ab* plane, which is a process considered as the trimerization of Mn^{3+} [7,8,9]. As a consequence, asymmetric displacement of Y^{3+} ions occurs, leading to the inequality of apical Y–O bond lengths and induction of electric dipole moments, electric polarization, and ferroelectricity [2]. These changes are attributed to the isosymmetric structural transition (the space-group symmetry and Wyckoff position occupations are preserved) at about 920 K, generated by a displacement of the manganese and oxygen ions in MnO_5 bipyramides [11,12]. This improper ferroelectric distortion ($P6_3cm \rightarrow P6_3cm$) induced a spontaneous electric polarization. $YMnO_3$ is a geometrically frustrated antiferromagnet with noncollinear Mn^{3+} spins arranged in so-called 120° spin structure, in which differently oriented

magnetic moments of Mn^{3+} ions, located at vertices of the triangle in *ab* plane, form 120º angles [10,13,14]. The spin of single Mn^{3+} is coupled with three spins existing in Mn^{3+} trimer occurring in neighboring layer, leading to zero total spin [3]. Antiferromagnetic ordering originates from in-plane Mn^{3+}–O^{2-}–Mn^{3+} superexchange interactions, while interplane Mn^{3+}–O^{2-}–O^{2-}–Mn^{3+} super-superexchange interactions enable stabilization of the three-dimensional magnetic structure [9,15–20].

The application possibilities of $YMnO_3$ ceramics are limited by persistent microstructure defects (microcracks and micropores), which certainly contribute to the unfavorable reduction of material density [21]. Microcracking is a consequence of internal stress, which occurs during cooling process from high sintering temperature to room temperature, due to strong anisotropy of thermal expansion in hexagonal unit cell, characterized by a large value of thermal expansion coefficient. The expansion of sample and reopening of microcracks occur during the cooling below microcracking temperature (about 620 °C). The microcracks also occur because of high-temperature phase transition at about 1000 °C, from centrosymmetric $P6_3/mmc$ to non-centrosymmetric $P6_3cm$ structure [8,21]. These microstuctural defects greatly affect the transport properties of material and lead to weakening of its ferroelectric response. The concentration of defects can be decreased by reducing the grain size below a critical value achieved through doping of the material.

The doping is one of the most common methods for modifying physical properties of *h*-$YMnO_3$. There is a number of studies about doping effect on *h*-$YMnO_3$ such as incorporation of Fe^{3+}, Cr^{3+}, Ga^{3+}, Ti^{4+}, Al^{3+}, In^{3+} at Mn^{3+} site [22,23,24,3,10, 25, 26], and Lu^{2+}, Zr^{4+}, Gd^{3+}, Dy^{3+} at Y^{3+} site [27,28,29,9]. The presence of dopant in $YMnO_3$ generally influences the unit cell volume and *c/a* ratio [3,8,25], and consequently affects antiferromagnetic and ferroelectric properties and magnetoelectric coupling [3,9,23,30].

Using titanium (Ti^{4+}) as a dopant could change structural, microstructural and multiferroic properties of $YMnO_3$. Similarity of ionic radii of Ti^{4+} (r = 0.51 Å, coordination number, CN = 5) and Mn^{3+} (r = 0.58 Å,CN = 5) allows the implementation of Ti^{4+} into $YMnO_3$ lattice [31]. The partial substitution of Mn^{3+} with Ti^{4+} should

decrease concentration of oxygen vacancies, suppress reduction of Mn^{3+} to Mn^{2+}, and also reduce the electrical conductivity of $YMnO_3$, enabling the detection of the materials ferroelectric response. Ti-doping of $YMnO_3$ should cause a decrease in the *c*/*a* ratio of the unit cell and in the grain size, leading to a reduction of the anisotropic thermal expansion [7,8,21,32].

The partial substitution of Mn^{3+} with Ti^{4+} in $YMnO_3$ resulted in the preparation of $YMn_{1-x}Ti_xO_{3+\delta}$. The δ symbol had to be introduced into the chemical formula due to the maintaining of charge balance, indicating the necessary presence of interstitial oxygen atoms after Ti^{4+} introduction into the system.

In this work, we investigated the impact of different Ti^{4+} concentrations (x = 0 – 0.20) on microporosity and microcracking, and elucidated its influence on structural, ferroelectric and magnetic properties of $YMn_{1-x}Ti_xO_{3+\delta}$ ceramics. For the first time, the sol-gel polymerization complex method, especially suitable for the synthesis of doped systems, was used for the synthesis of $YMn_{1-x}Ti_xO_{3+\delta}$ precursor powders. The predefined ratio of citric acid and ethylene glycol enabled the formation of the polyester network in which metal ions are uniformly distributed. As a result, homogeneous powders of controlled composition were obtained. Less energy and less time were invested in the sintering of the sol-gel prepared precursor powders in comparison with other synthesis methods (mostly, solid state synthesis method).

The aim was to determine the optimal composition leading to improved density and microstructure and, consequently, to the most pronounced magnetic and ferroelectric properties. Titanium was chosen as a dopant because the existing research indicated that Ti^{4+} insertion into the Mn^{3+}-site reduces the microcracks concentration [8,10]. The correlation between structural, microstructural, and multiferroic properties of $YMn_{1-x}Ti_xO_{3+\delta}$ ceramics was thoroughly explained depending on the dopant concentration.

2 Experimental section

2.1 *Preparation of ceramic powders and processing*

The samples of $YMn_{1-x}Ti_xO_{3+\delta}$ (x = 0, 0.04, 0.08, 0.10, 0.15, 0.20) were prepared using sol-gel polymerization complex (PC) method. Starting components were manganese(II) acetate tetrahydrate ($Mn(CH_3COO)_2 \cdot 4H_2O$, Sigma Aldrich, 99.99 %), yttrium nitrate hexahydrate ($Y(NO_3)_3 \cdot 6H_2O$, Alfa Aesar, 99.9 %), citric acid ($C_6H_8O_7 \cdot H_2O$, Lach-Ner, p.a.), ethylene glycol ($C_2H_6O_2$, Fluka, 99.5 %) and aqueous titania sols. For aqueous titania sols, 20.0 mmol of titanium(IV) tetraisopropoxide (TIPT, Alfa Aesar, 97 %) was slowly mixed with 20.0 mmol of acetylacetone (acac, Alfa Aesar, 99 %) under continuous (10 minutes) stirring at room temperature. The obtained turbid yellow TIPT/acac precursor was added dropwise to 50 ml of 0.40 M aqueous solution of acetic acid (CH_3COOH, Sigma Aldrich, 99.5 - 102.0 %) under continuous stirring, for 1 h, at room temperature, resulting in transparent yellow solution [33].

Precursor mixture containing $Mn(CH_3COO)_2 \cdot 4H_2O$, aqueous titania sols and citric acid (CA) in molar ratio Mn^{2+} : Ti^{4+} : CA = $(1 - x)$: x : 4 was mixed with 50 ml of distilled water in a boiling flask. The solution was heated and stirred under reflux at 60 °C, for 3 h. White precipitate of manganese citrate was produced and afterwards dissolved by adding aqueous NH_3 (NRK Inženjering, 25 %) until pH value of the solution reached 6. Ethylene glycol (EG) was added to this solution in a molar ratio Mn^{3+} : Ti^{4+} : CA : EG = $(1 - x)$: x : 4 : 30. $Y(NO_3)_3 \cdot 6H_2O$ was dissolved in EG and CA in a molar ratio Y^{3+} : CA : EG = 1 : 4 : 30. Yttrium and manganese/titanium solutions were combined (Y^{3+} : (Mn^{3+} + Ti^{4+}) = 1 : 1) in order to obtain precursor solutions, which were carefully heated for five days, until black precursor powder was produced. Their calcinations at 900 °C for 4 h (heating rate of 2 °/min) resulted in black $YMn_{1-x}Ti_xO_{3+\delta}$ (x = 0–0.20) powders. The $YMn_{1-x}Ti_xO_{3+\delta}$ powders were uniaxially pressed at a pressures of p = (2–6) t/cm^2 (196–588 MPa) into pellets (diameter of 8 mm). Sintering was carried out in chamber furnace under ambient atmosphere for 2 h at: 1400 °C for $YMnO_3$, $YMn_{0.96}Ti_{0.04}O_{3+\delta}$, $YMn_{0.92}Ti_{0.08}O_{3+\delta}$ and $YMn_{0.90}Ti_{0.10}O_{3+\delta}$ samples; 1450 °C for $YMn_{0.85}Ti_{0.15}O_{3+\delta}$, and 1470 °C for $YMn_{0.80}Ti_{0.20}O_{3+\delta}$.

2.2 *Characterization of ceramic samples*

Structural and phase composition analyses of pulverized ceramic samples were performed by X–ray diffractometer (PANalytical X`Pert PRO a1 MPD), using Cu–Kα1 radiation (λ = 1.54056 Å) and X'Celerator detector. Diffraction patterns were recorded at room temperature in the 2θ-range from 10° to 90° with a step of 0.034° and integration time 1 s per step for all samples. XRD patterns for $YMn_{1-x}Ti_xO_{3+\delta}$ (x = 0, 0.10, 0.15) samples recorded at room temperature in the range 2θ = (5–100)° with a step of 0.016° and integration time 1 s per step, were used for Rietveld refinement. *PowderCell* software was used to identify and determine the final phase composition [34] by performing Rietveld-like refinement in profile matching mode, while unit cell parameters were calculated using *LSUCRIPC* software [35]. The *FULLPROF* software was used for the Rietveld refinement in *WINPLOTR* environment on 5588 data points and 91 (for $YMnO_3$), 158 (for $YMn_{0.90}Ti_{0.10}O_{3+\delta}$) and 142 (for $YMn_{0.85}Ti_{0.15}O_{3+\delta}$) reflections [36,37]. The profiles were described by the pseudo-Voigt function as the most frequently used function in this type of analysis. In the first stage of the refinement, the background was modelled using a linear interpolation between 74 selected points, and in the last cycles the Fourier filtering method with the window size set to 4000 was used. The profile parameters, atomic positions and isotropic atomic displacement parameters were refined.

Microstructure of ceramic samples was observed using scanning electron microscopes (SEM) Tescan Vega TS 5130MM. Selected Area Electron Diffraction (SAED) analysis was performed using transmission electron microscope (TEM) Jeol JEM-2100. $YMn_{0.85}Ti_{0.15}O_{3+\delta}$ sample was prepared for the TEM analysis by cutting pellet into 3 mm disc using an ultrasonic cutter (SONICUT380, SBT, USA) and pellet was further mechanically thinned to 100 μm. The disc was then dimpled down to 20 μm in the centre (Dimple grinder 656, Gatan Inc., USA), and then ion-milled (PIPS 691, Gatan Inc., USA) using 4 kV Ar^+ ions at an incidence angle of 8° to obtain large transmissive areas for the TEM investigations. Precision Multiferroic Test System (Radiant Technologies, Inc.) was used for measuring the ferroelectric hysteresis curves and leakage currents. Measurements were carried out on pellets coated with gold electrodes, in TDC mode (Compensating for Time Dependent Charge Components in

Hysteresis Loops), with hysteresis periods equal to 10 ms and 20 ms. Field dependence of magnetization was measured in fields up to 50 kOe (5 T) at 3 K, 30 K and 50 K using commercial MPMS5 SQUID magnetometer. Measurements of the zero-field-cooled (ZFC) and field-cooled (FC) temperature dependence of magnetization were carried out in constant applied fields (10 Oe and 1000 Oe) in temperature range (2–400) K. Pellets were inserted directly into the measuring straw, so there is no magnetic contribution of the background.

3 Results and discussion

The influence of Ti-doping on structure of $YMnO_3$ can be analysed from XRD patterns of $YMn_{1-x}Ti_xO_{3+\delta}$ (x = 0, 0.04, 0.08, 0.10, 0.15, and 0.20) pulverized ceramic samples (Fig. 1). The samples with x = 0 and 0.04 crystallized in space group $P6_3cm$ with the structure typical for hexagonal $YMnO_3$ (PDF # 25-1079). The disappearance of some reflections characteristic for h-$YMnO_3$ (positioned at 2θ = 22.9°, 35.8°, 46.8°, 48.0°, 67.9°, 73.2º, 75.7º, 83.3º, 85.4º) and the appearance of new ones (positioned at 26.9°, 35.0º, 48.7º, 63.7º, 82.0º, 84.1º) implied a structural transition for samples with $x \geq 0.08$. Their phase composition analysis showed transition from the single phased hexagonal structure to the rhombohedral 1×1×3 superstructure with $R3c$ space group [38]. $YMn_{0.92}Ti_{0.08}O_{3+\delta}$ and $YMn_{0.90}Ti_{0.10}O_{3+\delta}$ samples consisted of two phases, one with hexagonal structure and the other with rhombohedral 1×1×3 superstructure (Table 1). The samples with x = 0.15 and 0.20 are single-phased and crystallized in rhombohedral 1×1×3 superstructure. Although rhombohedral structure could be represented by either rhombohedral or hexagonal axes, we used hexagonal axes to compare these two structures. The several reflections of both phases coincide at the certain 2θ positions for $YMn_{0.92}Ti_{0.08}O_{3+\delta}$ and $YMn_{0.90}Ti_{0.10}O_{3+\delta}$ samples. These results differ from previously reported in literature [8,10], which were related to $YMn_{1-x}Ti_xO_3$ ($0 \leq x \leq 0.25$) samples prepared by solid-state reaction. It was reported that the appearance of another phase occurs in the samples with $x \geq 0.15$, and that the rhombohedral phase becomes dominant in the samples with $x > 0.30$. In our work, using different synthetic procedure (PC), the

single phase sample with stable superstructure was obtained at much lower Ti concentration. It is obvious that the PC method has an advantage over the solid state method because it provides a more uniform distribution of metal ions in the formed polyester network, which achieves *R*3*c* superstructure ordering in $YMn_{1-x}Ti_xO_3$ at lower concentrations of Ti^{4+}.

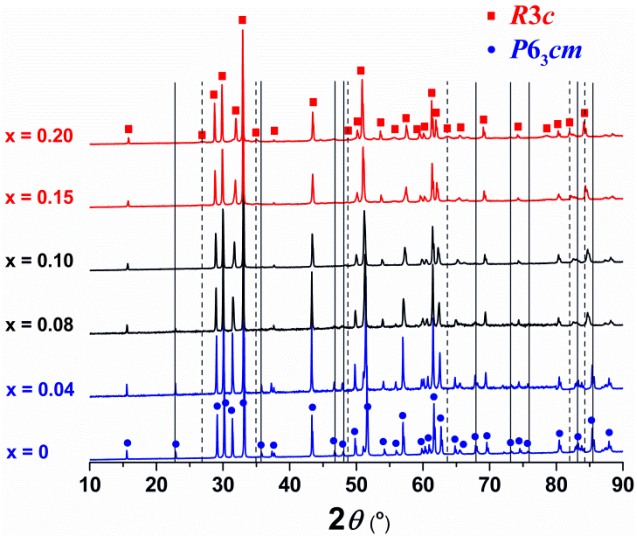

Fig. 1 (*color online*) The X-ray diffraction patterns of $YMn_{1-x}Ti_xO_{3+\delta}$ (x = 0; 0.04; 0.08; 0.10; 0.15; 0.20) pulverized ceramic samples (The disappeared reflections characteristic for *h*-$YMnO_3$ ($P6_3cm$) are marked by verical solid lines, and the reflections unique to the rhombohedral $YMnO_3$ ($R3c$) by a vertical dashed lines.)

Unit cell parameters of $YMn_{1-x}Ti_xO_{3+\delta}$ (x = 0–0.20) samples are shown in Table 1. The calculated unit cell parameters for undoped $YMnO_3$ sample (a_H = 6.131(7) Å, c_H = 11.395(8) Å) are consistent with literature data (PDF # 25-1079). For doped samples with $x < 0.15$, the value of in-plane lattice parameter, a_H, increased and the value of out-of-plane lattice parameter, c_H, decreased, with increase in Ti concentration (Fig. 2). The change of c_H after incorporation of Ti^{4+} in $YMnO_3$ could be attributed to the difference in ionic radii between Ti^{4+} and Mn^{3+}, and a minor distortion of the unit cell. Unit cell parameters of 1×1×3 superstructure, a_R and c_R, for samples with $x \geq 0.08$, followed the same trend as parameters of hexagonal unit cell i.e. a_R increased, while c_R decreased with increase of x.

Table 1 Unit cell parameters, the ratio c_H/a_H, relative densities (ρ/ρ_{theor}) and phase composition (wt.%) of $YMn_{1-x}Ti_xO_{3+\delta}$ (x = 0; 0.04; 0.08; 0.10; 0.15; 0.20) samples.

x	a (Å)	c (Å)	$c_H/a_{H(R)}$*	$V_{(H)}$ (Å^3)	ρ/ρ_{theor} (%)	$YMn_{1-x}Ti_xO_{3+\delta}$ ($P6_3cm$) (wt.%)	$YMn_{1-x}Ti_xO_{3+\delta}$ ($R3c$) (wt.%)
0	6.131(7)	11.395(8)	1.8586	371.0(7)	75	100	0
0.04	6.145(8)	11.389(9)	1.8534	372.4(8)	74	100	0
0.08	6.160(7)	11.336(7)	1.8403	372.5(7)	84	43	57
	6.168(7)	33.99(2)		1120(2)			
0.10	6.176(5)	11.304(6)	1.8303	373.4(5)	95	22	78
	6.178(6)	33.90(2)		1121(2)			
0.15	6.192(6)	33.64(2)	1.8109	1117(2)	93	0	100
0.20	6.207(7)	33.62(2)	1.8055	1122(2)	92	0	100

*The values of c_H parameter for $YMn_{0.85}Ti_{0.15}O_{3+\delta}$ and $YMn_{0.80}Ti_{0.20}O_{3+\delta}$ are obtained as one third of calculated values for c_R parameter.

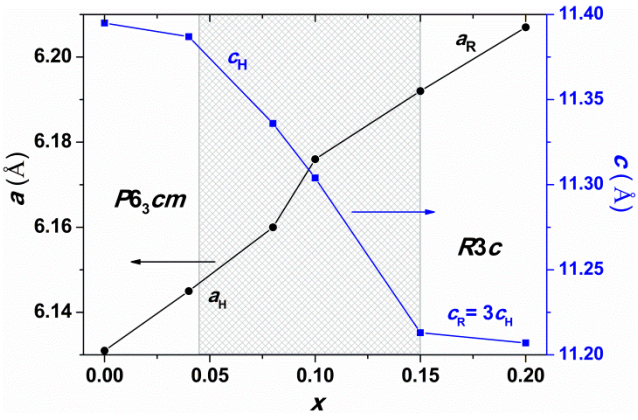

Fig. 2 (*color online*) Unit cell parameters (a_H, c_H) versus Ti concentration (x) for $YMn_{1-x}Ti_xO_{3+\delta}$ (x = 0; 0.04; 0.08; 0.10; 0.15; 0.20) samples. Hatched area shows the x-range of the hexagonal to the rhombohedral phase transition

The structural analysis was performed on samples with x = 0, 0.10 and 0.15 (Fig. S1 in ESM). The results of Rietveld refinement indicated single phase with hexagonal structure for undoped $YMnO_3$, and single phase with rhombohedral 1×1×3

superstructure with lattice parameters $a_R = a_H$, $b_R = b_H$ and $c_R = 3c_H$ for $YMn_{0.85}Ti_{0.15}O_{3+\delta}$ sample. The presence of two phases, one with hexagonal structure and the other with rhombohedral 1×1×3 superstructure, was confirmed for $YMn_{0.90}Ti_{0.10}O_{3+\delta}$, but the structural analysis was performed only for rhombohedral phase since it was the dominant one. The decrease of calculated values for angle between O3–O4 bond (in-plane oxygen) and the *ab* plane (Fig. 3) with increase of Ti-concentration is an indicator of reduction in tilting of MnO_5 bipyramids. It is in accordance with the increase of $a_{H(R)}$ and $b_{H(R)}$ parameters, and the decrease of $c_{H(R)}$ parameter. According to the obtained atomic positions (Table S1 in ESM), Mn–Mn distances and bond angles in the *ab* plane (i.e., Mn–O3–Mn, Mn–O4–Mn, Mn–O5–Mn) were also calculated. These structural parameters are of special interest because they determine the magnetic behavior of system. It is obvious that the Ti-doping led to increase in Mn–O–Mn bond angles and Mn–Mn distances, which are also indicators of prevailing decrease in geometrical frustration of triangular lattice in doped samples, as it will be explained through discussion of magnetic results.

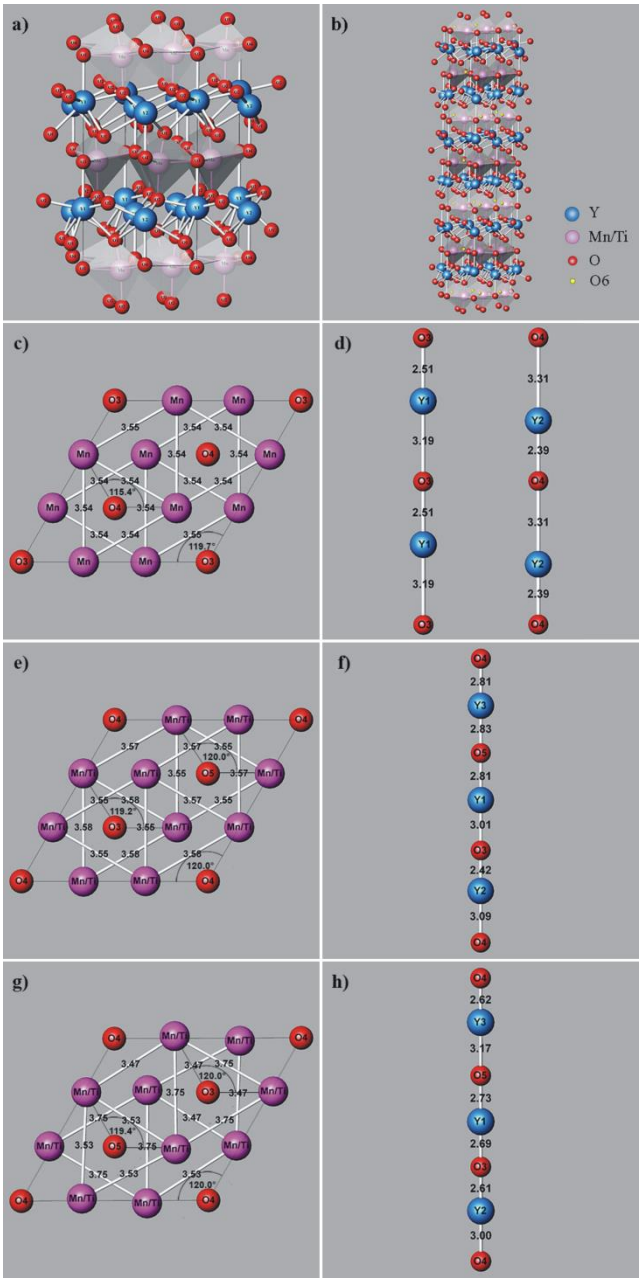

Fig. 3 (*color online*) Visualization of unit cells for: (a) $YMnO_3$, (b) $YMn_{0.90}Ti_{0.10}O_{3+\delta}$ and $YMn_{0.85}Ti_{0.15}O_{3+\delta}$. (O6 is an interstitial oxygen introduced due to charge balance). The arrangement of manganese and oxygen ions in *ab* plane and specified values of Mn–Mn distances and Mn–O–Mn bond angles for: (c) $YMnO_3$, (e) $YMn_{0.90}Ti_{0.10}O_{3+\delta}$ and (g) $YMn_{0.85}Ti_{0.15}O_{3+\delta}$. The values of Y–O bond lengths along *c*-axis for: (d) $YMnO_3$, (f) $YMn_{0.90}Ti_{0.10}O_{3+\delta}$ and (h) $YMn_{0.85}Ti_{0.15}O_{3+\delta}$

The confirmation of presence of the rhombohedral phase in $YMn_{0.85}Ti_{0.15}O_{3+\delta}$ sample was obtained using SAED technique. SAED patterns of $YMn_{0.85}Ti_{0.15}O_{3+\delta}$ sample were recorded along different zone axes (Fig. 4 a,b). Identification of (*hkl*) was carried out by observing the values of interplanar distance. Diffraction spots on electron diffraction patterns of $YMn_{0.85}Ti_{0.15}O_{3+\delta}$ were indexed according to 1×1×3 rhombohedral unit cell notation. [010] and $[1\bar{1}0]$ zone axes directions were determined by indexed spots. In order to confirm these results, the angle between (306) and (006) planes was measured. The obtained angle of 73° perfectly corresponded to angle calculated from the simulated 1×1×3 structure (73°). Namely, since the structural data for 1×1×3 do not exist in literature, we used simple hexagonal structure (ICSD #238967 and PDF#25-1079) to build 1×1×3 and also to transform unit cell from $P6_3cm$ to $R3c$ space group and to obtain corresponding reflection indices. The angles between set of planes (113) and (0012), and (0012) and (119) also corresponded well with rhombohedral phase (72° to 75°, and 50° to 51°, respectively) (Fig. 4b).

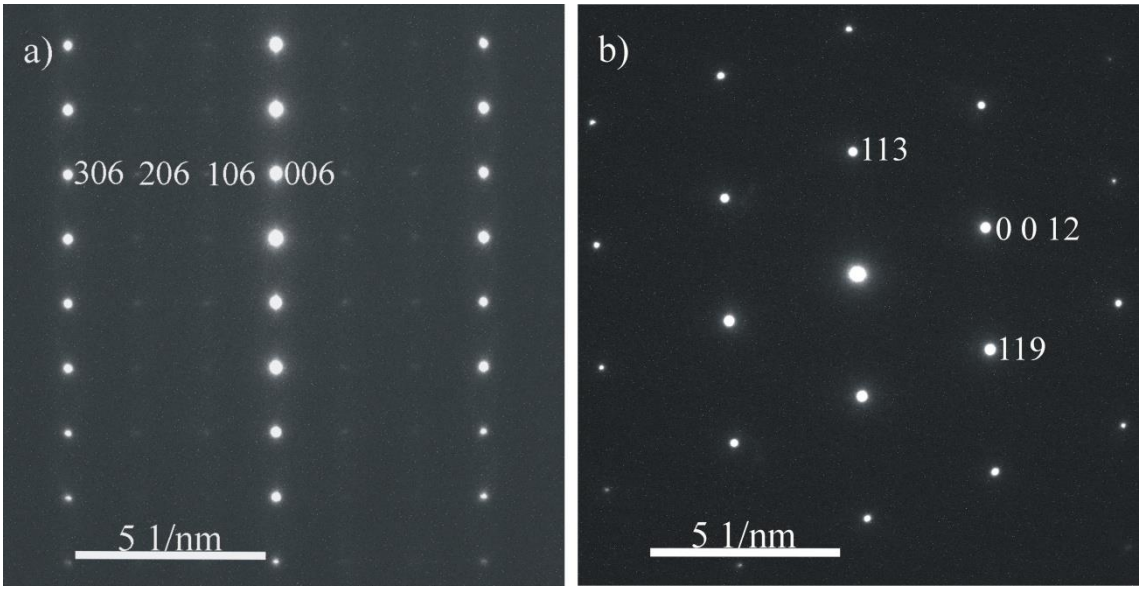

Fig. 4 SAED patterns for $YMn_{0.85}Ti_{0.15}O_{3+\delta}$ in: (a) [010] and (b) $[1\bar{1}0]$ zone axes

SEM micrographs presented in Fig. 5 reveal the influence of Ti doping on $YMnO_3$ microstructure. All $YMn_{1-x}Ti_xO_{3+\delta}$ ceramic samples had nonuniformly shaped grains with broad grain size distributions. It lied in the range of (4–12) μm (Fig. 5a) in $YMnO_3$, while doping with lower Ti concentrations (x = 0.04, 0.08) narrowed the range of grain size to (1–8) μm (Fig. 5 b,c). Increase of the dopant concentration along with the increase of sintering temperature broadened again the grain size within the range of (1–12) μm (Fig. 5 d,e,f). Microstructure of undoped $YMnO_3$ was poor with large number of microcracks and inter- and intragranular pores (Fig. 5a). It is obvious that microcracking process was suppressed with increase in Ti concentration and being diminished in the ceramic samples with $x \geq 0.10$. The presence of inter- and intragranular pores changed in the same manner – it is the number of pores significantly reduced in samples with higher Ti concentration, especially in $YMn_{0.20}Ti_{0.80}O_{3+\delta}$, in comparison with the undoped sample. These observations are also consistent with the lowering of c_H/a_H ratio of hexagonal unit cell when x increases (Table 1), which indicates decrease of thermal expansion anisotropy for hexagonal structure, as the one of the causes of microcracking occurrence.

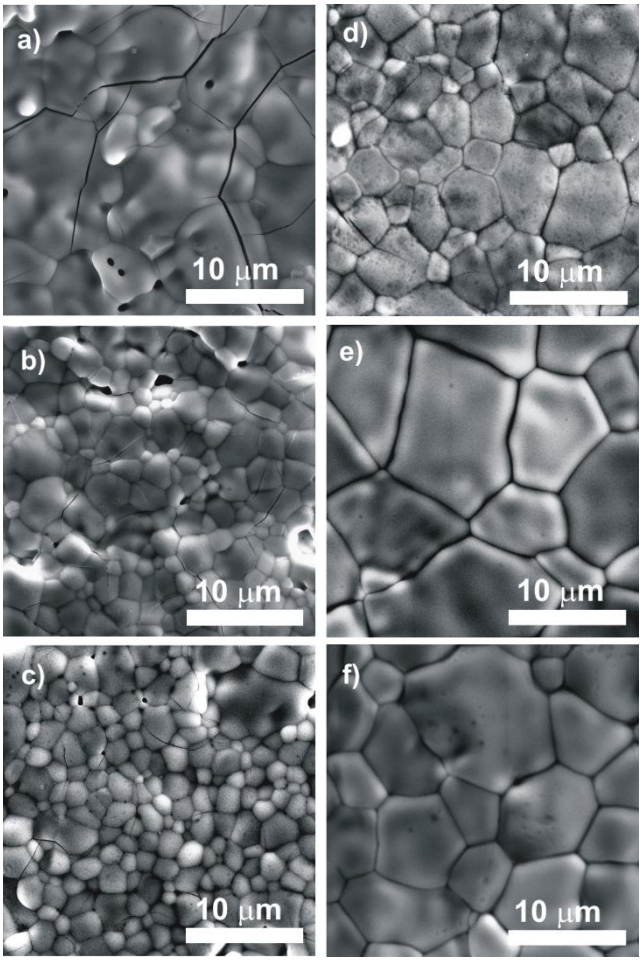

Fig. 5 SEM micrographs of the surface of $YMn_{1-x}Ti_xO_{3+\delta}$ ceramic samples: (a) $x = 0$, (b) $x = 0.04$, (c) $x = 0.08$, (d) $x = 0.10$, (e) $x = 0.15$ and f) $x = 0.20$

The reduction in microcracks' and pores' concentration was also reflected on relative density of samples (Table 1). The increase in Ti concentration required a higher sintering temperature, which led to improved densification of ceramics and higher relative density of the samples. It can be considered that the difficulty related to densification process of the material [39] is mitigated through the sintering temperature optimization. The presence of microstructural defects is usually reflected on the ferroelectric behavior of $YMnO_3$ ceramics. Therefore, the reduction of microcracks and micropores after Ti-doping [8,21] should facilitate the observation of ferroelectric response.

The lattice distortion, as a consequence of tilting of MnO_5 bipyramides toward O3 and buckling of Y^{3+} layers, resulted in the existence of two Y^{3+}–O^{2-} bonds (for each

Y^{3+}) along *c*-axis with different bond lengths (Fig. 3 d, f, h) [15]. Accordingly, Y1–O3 and Y2–O4 bonds are observed in the undoped sample, while Y1–O3, Y1–O5, Y2–O3, Y2–O4, Y3–O4, Y3–O5 bonds are considered in Ti-doped samples. The displacements of Y^{3+} and oxygen ions in opposite directions generated electric dipole moments along *c*-axis and led to the occurrence of electric polarization, *P* measured in the applied electric field, *E*. *P*(*E*) hysteresis loops of all samples indicated that saturation was not achieved in applied electric fields (Fig. 6), but still for easier description and explanation we will use the terms– apparent remnant polarization (P_r^a), and apparent coercive field (E_c^a). Sharp hysteresis form and low value of P_r^a pointed out weak and poor ferroelectric response of $YMnO_3$. The samples with x = 0.04 and 0.08 showed lower values of P_r^a and the inrease of E_c^a. $YMn_{0.90}Ti_{0.10}O_{3+\delta}$ sample exhibited slightly higher value of P_r^a and larger value of E_c^a than $YMnO_3$ sample. It is also noticeable that samples with x = 0.04, 0.08 and 0.10 showed certain tendency to "flattening" of *P*(*E*) curves (in the endpoints). Further increase of Ti concentration led to deterioration of ferroelectric characteristics and the samples with x = 0.15 and 0.20 exhibited dielectric-like behavior.

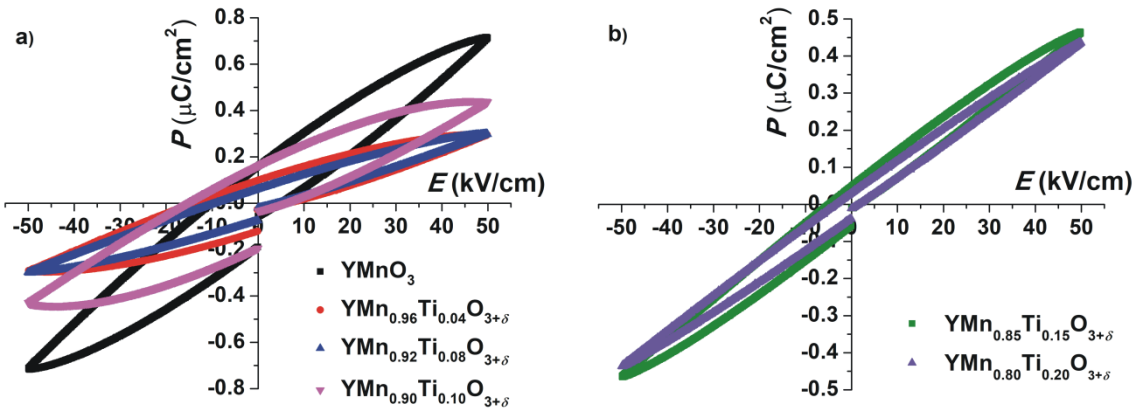

Fig. 6 (*color online*) Room temperature *P*(*E*) curves of $YMn_{1-x}Ti_xO_{3+\delta}$ samples in applied electric field *E* = 50 kV/cm at the frequencies of 100 Hz and 50 Hz for: (a) x = 0; 0.04; 0.08; 0.10, (b) x = 0.15; 0.20

The absence of square ferroelectric hysteresis curves was consistent with the presence of large leakage currents in samples. The doping with titanium mainly resulted in small reduction of leakage currents (Fig. 7). It is assumed that oxygen vacancies' concentration was decreased due to the partial substitution of Mn^{3+} with Ti^{4+} and, consequently, it suppressed leaky behavior to a certain extent. However, this trend did not show regularity in relation to dopant concentration. Besides, the effect of relative density and porosity of samples on their ferroelectric properties and leaky behavior, which we expected, was not observed. Considering the results from the literature related to $YMnO_3$ based ceramics [40,41], it can be concluded that the obtained ferroelectric response of $YMn_{1-x}Ti_xO_{3+\delta}$ ceramic samples presented in our work is stronger and better defined in a wider range of electric field compared with the results of others. As expected, the ferroelectric response of the $YMnO_3$ single crystal is incomparably stronger and it has a regular hysteresis form [42].

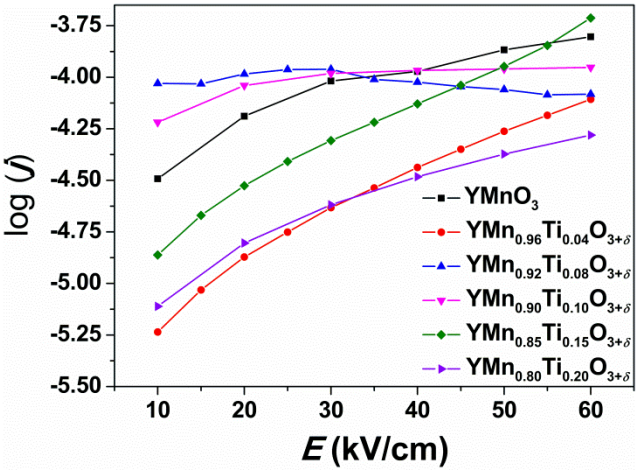

Fig. 7 (*color online*) Leakage current density (*j*) versus applied electric field (*E*) curves for $YMn_{1-x}Ti_xO_{3+\delta}$ ($0 \le x \le 0.20$) ceramic samples

Despite the reduction of microstuctural defects and electric conductivity in doped samples, their ferroelectric responses were not significantly improved. In fact, the introduction of Ti^{4+} in the place of Mn^{3+} (not instead of Y^{3+}) caused such displacements of the ions that resulted in decrease of electric polarization of crystal lattice. Obviously,

the impact of reduction of the lattice distortion surpassed the effect of improved microstructural properties on the ferroelectric response of samples. Accordingly, we can conclude that the influence of structural properties on the (ferro)electric properties of the samples dominated over the influence of their microstructural properties.

Ti-doping had a significant impact on magnetic properties of $YMnO_3$. In high temperature region, the paramagnetic behavior of prepared materials was observed, and expectedly the ZFC- and FC- $M(T)$ curves overlapped. The slight bifurcation between these two curves occurred at low temperatures (Fig. 8), indicating magnetic irreversibility in the ordered phase. The combination of antiferromagnetic and weak ferromagnetic behavior could be presumed from these curve shapes. Increase of magnetization and larger separation of ZFC- and FC-$M(T)$ curves for $YMn_{0.90}Ti_{0.10}O_{3+\delta}$, $YMn_{0.92}Ti_{0.08}O_{3+\delta}$ and $YMn_{0.85}Ti_{0.15}O_{3+\delta}$ indicated growth of the weak ferromagnetic moments. The origin of weak ferromagnetism has been explained as a consequence of Mn spins canting, which produces small resulting magnetic moment along the *c*-axis [43].

The Néel temperatures for $YMn_{1-x}Ti_xO_{3+\delta}$ samples (Table 2) were estimated according to the position of point at which the splitting between the ZFC-$M(T)$ and FC-$M(T)$ curves began (measured in H = 10 Oe). They represent the transition temperatures below which the antiferromagnetic ordering appears, and, for doped samples, they are all lower than literature value of the Néel temperature for $YMnO_3$ (T_N = 70 K). The temperature lowering could come from the disorder of the ideal magnetic lattice and competition between the disordering and establishing of new interactions after the Ti substitutions.

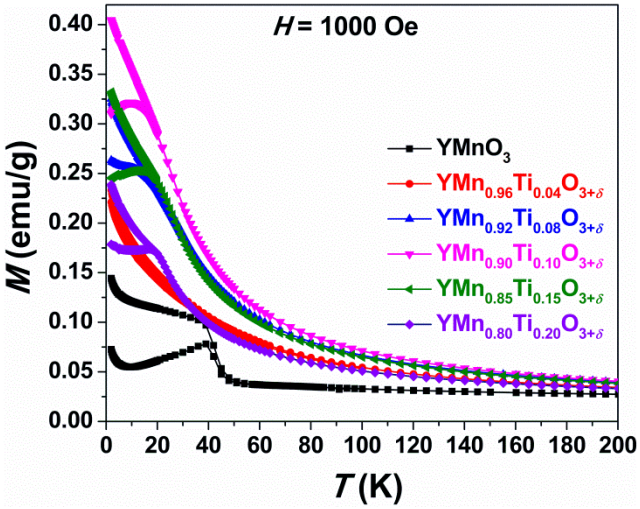

Fig. 8 (*color online*) Temperature dependences of zero-field-cooled and field-cooled magnetization for $YMn_{1-x}Ti_xO_{3+\delta}$ (x = 0, 0.04, 0.08, 0.10, 0.15, 0.20) samples, measured in the magnetic field of 1000 Oe

High temperature region of magnetic susceptibility $\chi=M/H$ is fitted by the Curie-Weiss law $\chi=C/(T-\theta)$ using the linear part of $1/\chi(T)$ curves. Weiss parameter ($|\theta|$) was estimated as the intercept of $1/\chi(T)$ curve on T-axis and effective magnetic moment (μ_{eff}) was calculated using $\mu_{eff} = 2.828\,(C)^{1/2}\mu_B$ formula, where C is Curie constant obtained from the slope of $1/\chi(T)$, for each sample (Table 2). The values of Weiss parameter are related to the average (super)exchange interactions between Mn^{3+} spins necessary for the (anti)ferromagnetic arrangement. The partial substitution resulted generally in decrease of $|\theta|$ if compared with undoped $YMnO_3$, indicating considerable reduction of the mean-field averaged superexchange interactions between Mn^{3+} magnetic moments after Ti^{4+} insertion. The values of T_N and μ_{eff} of doped samples also significantly decreased after partial substitution of Mn^{3+} ions with nonmagnetic Ti^{4+} ions, being in agreement with reduction of superexchange interactions and lowered amount of paramagnetic centres. The discrepancy between values of T_N and $|\theta|$ originated from strong geometrically frustrated spins in the manganese triangular lattice in the *ab* plane as a consequence of the antiferromagnetic fluctuations of Mn^{3+} spins that inhibit the formation of long range magnetic ordering in the system [10,44]. The decrease of $|\theta|$ and μ_{eff} could be explained by weakening of Mn^{3+} ions trimerization (weakening of geometrical frustration) and suppression of strong and strict antiferromagnetic ordering in Ti-substituted $YMnO_3$. A more detailed structural study with neutron diffraction has

shown that analogous substitutions with non-magnetic ions produced large canting of the spins from the basal plane and influenced the order in similar manner [45].

Frustration parameter (f), as a measure of geometrical frustration of antiferromagnetic system, is defined as ratio of the Weiss constant and Néel temperature, $|\theta|/T_N$ [20]. It ranged from 3.63 for $YMnO_3$ to 0.9 for $YMn_{0.90}Ti_{0.10}O_{3+\delta}$ (Table 2), indicating that Ti-doping up to x = 0.10 reduced geometrical frustration of triangular lattice and therefore strict antiferromagnetic ordering. Obviously, nonmagnetic Ti^{4+} in crystal lattice partially broke superexchange interaction path between Mn^{3+} ions that resulted in the decrease of T_N, $|\theta|$ and f altogether. Increase of the parameter f above this concentration is not easy to analyse and understand, due to the stronger structural changes induced with higher doping. Deeper understanding of such phenomena is missing and therefore calls for some advanced microscopic magnetic study rarely done for substituted systems [46].

Table 2 The values of Néel temperature (T_N), Weiss parameter ($|\theta|$), frustration parameter (f) and effective magnetic moment (μ_{eff}) for $YMn_{1-x}Ti_xO_{3+\delta}$ (x = 0, 0.04, 0.08, 0.10, 0.15, 0.20) samples.

x	T_N [K]	$\|\theta\|$ [K]	f	μ_{eff} [μ_B]
0	80 ± 1	290.3 ± 0.6	3.63 ± 0.06	3.800 ± 0.003
0.04	60 ± 1	103 ± 2	1.72 ± 0.07	3.699 ± 0.008
0.08	24 ± 1	36.7 ± 0.4	1.53 ± 0.09	3.558 ± 0.003
0.10	43 ± 1	38.6 ± 0.6	0.90 ± 0.04	3.623 ± 0.004
0.15	22 ± 1	46.2 ± 0.2	2.1 ± 0.2	3.561 ± 0.002
0.20	20 ± 1	77.4 ± 0.4	3.9 ± 0.3	3.478 ± 0.003

Hysteresis curves $M(H)$ measured at 3 K and 30 K are shown in Fig. 9. Magnetization of $YMnO_3$ exhibited nearly linear $M(H)$, with small magnetization, indicating antiferromagnetic-like behavior at 3 K and 30 K. $M(H)$ curves, measured at 3 K and 30 K, for $YMn_{1-x}Ti_xO_{3+\delta}$ (x = 0.04, 0.08, 0.10, 0.15, 0.20) samples, have higher magnetization at 5 T field than the $YMnO_3$, but still small, ranging from 0.25 to

0.4 Bohr's magneton (μ_B) per Mn^{3+} ion, in comparison with 0.08 μ_B for pure $YMnO_3$. Besides being far from saturation (4μ_B per Mn^{3+} ion), $M(H)$ curves showed a tiny bending at high fields. At 3 K, all doped samples showed relatively large coercive field of order of 1000 Oe (inset in Fig. 9a), similar to pure $YMnO_3$. Obviously, the Ti-substitutions did not increase the magnetic hardness, showing that the domain wall dynamics is inherent to magnetic system of $YMnO_3$. There is no drastic difference in microstructure between the differently substituted samples, therefore no drastic change of their magnetic hysteresis loops appeared. On the other hand, the amount of magnetization grew expectedly due to breaking the frustrated magnetic lattice, which had antiferromagnetic ground state, and introduction of uncompensated magnetic moments. Besides increasing the magnetization, Ti-substitution enhanced weak ferromagnetism due to breaking the symmetry of superexchange bridges, which increased the spin canting. Namely, the partial substitution of Mn^{3+} with Ti^{4+} led to increase in Mn–O–Mn bond angles (Fig. 3 c,e,g) and, consequently, to weakening of superexchange interaction responsible for predominantly antiferromagnetic ordering, and enhancing the possible Dzyaloshinskii-Moriya term at the same time. That is visible in lowering of T_N and in enhancing the anti-symmetric exchange interaction between magnetic ions responsible for spin canting and weak ferromagnetism. At 30 K, coercivity of substituted samples diminished for one order of magnitude contrary to undoped compound (inset in Fig. 9b), that is in agreement with approaching to the lowered phase transition temperature of the substituted compounds. The magnetic moments per formula units cannot be determined from saturation values of $M(H)$ curves at low temperatures, but effective moments can be deduced from the slopes of $M(H)$ curves above magnetic transition, being in agreement with relatively small values obtained from $M(T)$ analysis. Our results indicated the weak ferromagnetic behavior below the appropriate Néel temperature, most pronounced in $YMn_{0.90}Ti_{0.10}O_{3+\delta}$ ceramic sample, which makes it the favourable candidate for thin films applicable in spintronics.

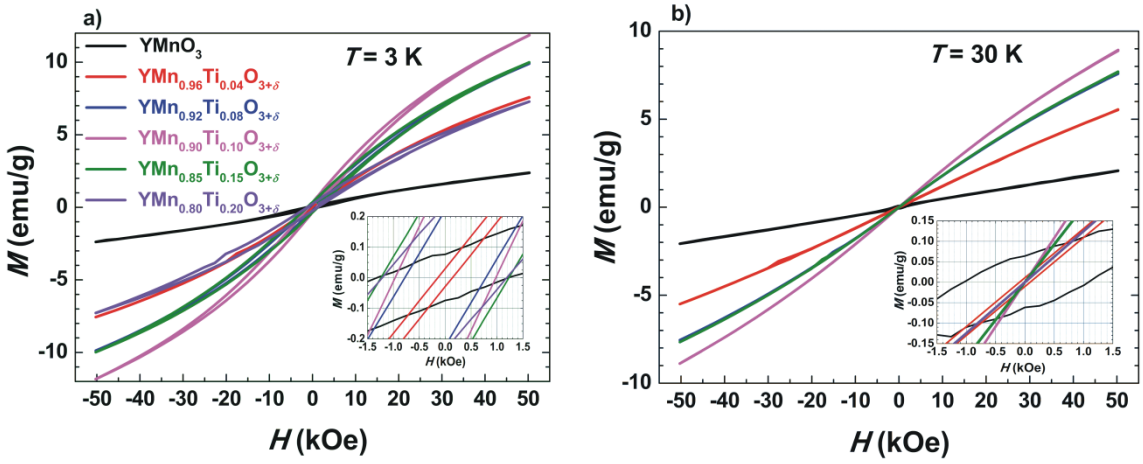

Fig. 9 (*color online*) Magnetic hysteresis curves $M(H)$ for $YMn_{1-x}Ti_xO_{3+\delta}$ (x = 0, 0.04, 0.08, 0.10, 0.15, 0.20) ceramic samples at: (a) 3 K and (b) 30 K

The decrease of c_H, as out-of-plane lattice parameter, is a consequence of prevailing reduction in geometrical frustration when concentration of Ti^{4+} increases. Ti-doping also caused a change of Mn–Mn distances, Y–O bond lengths and Mn–O–Mn bond angles in a manner that confirms the reduction of crystal lattice distortion and trimerization of Mn ions (Fig. 3). The trend of their change is not completely regular, but it is obvious enough, and the irregularities might come from the defects and inhomogeneities in the polycrystalline systems. The increase of Mn–Mn distances and Mn–O–Mn bond angles for a series of concentrations $x = 0, 0.10, 0.15$ caused the weakening of superexchange interaction (reflected in reduced Néel temperature) and the strengthening of weak ferromagnetic coupling of spins (reflected in increased magnetization).

4 Conclusions

$YMn_{1-x}Ti_xO_{3+\delta}$ (x = 0, 0.04, 0.08, 0.10, 0.15, 0.20) ceramic samples obtained by polymerization complex method were investigated in terms of their structural, microstructural, ferroelectric and magnetic characteristics. The correlation between the

structural/microstructural properties and magnetic/ferroelectric characteristics of $YMn_{1-x}Ti_xO_{3+\delta}$ ceramics was elucidated during this research. Ti-substitution in $YMnO_3$ was accompanied with structural transition from hexagonal ($P6_3cm$) structure to rhombohedral ($R3c$) superstructure, starting from x = 0.08. The partial substitution of Mn^{3+} with Ti^{4+} in $YMnO_3$ led to decrease of microcracks and pore density. Ti-doping also affected ferroelectric and, especially, magnetic behavior of investigated samples. $YMn_{1-x}Ti_xO_{3+\delta}$ samples mostly exhibited a reduction in leakage currents, but ferroelectric response was not significantly improved. The results of magnetic measurements showed that incorporation of nonmagnetic Ti^{4+} in $YMnO_3$─broke exchange paths and increased Mn–Mn distances and Mn–O–Mn bond angles, leading to suppression of antiferromagnetic ordering. It was also accompanied with lowering of the Néel temperature and weakening of Mn^{3+} trimerization, resulting in considerable increase of magnetization. The certain enhancement of magnetic response after Ti-doping of $YMnO_3$ could be exploited for practical use. The optimal dopant concentration was achieved in $YMn_{0.90}Ti_{0.10}O_{3+\delta}$, because this sample had the highest relative density, and it exhibited slightly stronger ferroelectric response as well as the largest magnetic response.

Acknowledgments

The authors acknowledge the financial support of the Ministry of Education, Science and Technological Development of the Republic of Serbia (Contract No. 451-03-68/2022-14/200053 and 451-03-9/2022-14/200135). We also acknowledge support from the COST Action grant number CA17123 - MAGNETOFON. The TEM work was conducted in the infrastructure of Centre for Electron Microscopy and Microanalysis (CEMM) in Jožef Stefan Institute, Ljubljana, Slovenia. D. Pajić and P. Šenjug acknowledge the support of project CeNIKS co-financed by the Croatian Government and the European Union through the European Regional Development Fund - Competitiveness and Cohesion Operational Programme (Grant KK.01.1.1.02.0013).

Conflict of interest The authors declare that they have no conflict of interest.

References

[1] McBean CL, Lewis CS, Tiano AL, Simonson JW, Han MG, Gannon WJ, Yue S, Patete JM, Corrao AA, Santulli AC, Wu L, Aronson MC, Zhu Y, Wong SS (2017) A generalizable multigram synthesis and mechanistic investigation of $YMnO_3$ nanoplates. Ind Eng Chem Res 56:5573–5585. https://doi.org/10.1021/acs.iecr.7b00113.

[2] Polat O, Coskun M, Coskun FM, Durmus Z, Caglar M, Turut A (2018) Os doped $YMnO_3$ multiferroic: A study investigating the electrical properties through tuning the doping level. J Alloy Compd 752:274–288. https://doi.org/10.1016/j.jallcom.2018.04.200.

[3] Nugroho AA, Bellido N, Adem U, Nénert G, Simon Ch, Tjia MO, Mostovoy M, Palstra TTM, Enhancing the magnetoelectric coupling in $YMnO_3$ by Ga doping (2007) Phys Rev B 75:174435. https://doi.org/10.1103/PhysRevB.75.174435.

[4] Wang T, Song SH, Ma Q, Tan ML, Chen JJ (2019) Highly improved multiferroic properties of Sm and Nb co-doped $BiFeO_3$ ceramics prepared by spark plasma sintering combined with sol-gel powders. J Alloy Compd 795:60-68. https://doi.org/10.1016/j.jallcom.2019.04.327.

[5] Zhang M, Zhang X, Qi X, Zhu H, Li Y, Gu Y (2018) Enhanced ferroelectric, magnetic and magnetoelectric properties of multiferroic $BiFeO_3$–$BaTiO_3$–$LaFeO_3$ ceramics. Ceram Int 44:21269–21276. https://doi.org/10.1016/j.ceramint.2018.08.175.

[6] Počuča-Nešić M, Marinković Stanojević Z, Branković Z, Cotič P, Bernik S, Sousa Góes M, Marinković BA, Varela JA, Branković G (2013) Mechanochemical synthesis of yttrium manganite. J Alloy Compd 552:451–456. https://doi.org/10.1016/j.jallcom.2012.11.031.

[7] Kumara M, Phase DM, Choudhary RJ, Upadhyay SK, Reddy VR (2018) Microwave assisted radiant hybrid sintering of $YMnO_3$ ceramic: Reduction of microcracking and

leakage current. Ceram Int 44:8196–8200. https://doi.org/10.1016/j.ceramint.2018.01.268.

[8] Tomczyk M, Senos AMOR, Reaney IM, Vilarinho PM (2012) Reduction of microcracking in $YMnO_3$ ceramics by Ti substitution. Scripta Mater 67:427–430. https://doi.org/10.1016/j.scriptamat.2012.04.042.

[9] Muneeswaran M, Jang JW, Choi BC, Jeong JH, Giridharan NV (2017) Structural, optical and multiferroic properties of pure and Dy modified $YMnO_3$. J Mater Sci-Mater El 28:16788–16796. https://doi.org/10.1007/s10854-017-7593-z.

[10] Durán A, Guzmán G, Ochoa-Guerrero CI, Herbert C, Escudero R, Morales F, Escamilla R (2019) Ti-doped $YMnO_3$: Magnetic and thermal studies at low temperature and dielectric properties at high temperature. J Appl Phys 125:034102. https://doi.org/10.1063/1.5055228.

[11] Lonkai Th, Tomuta DG, Amann U, Ihringer J, Hendrikx RWA, Többens DM, Mydosh JA (2004) Development of the high-temperature phase of hexagonal manganites. Phys Rev B 69:134108. https://doi.org/10.1103/PhysRevB.69.134108.

[12] Gibbs AS, Knight KS, Lightfoot P (2011) High-temperature phase transitions of hexagonal $YMnO_3$. Phys Rev B 83:094111. https://doi.org/10.1103/PhysRevB.83.094111.

[13] Vaz CAF, Hoffman J, Ahn CH, Ramesh R (2010) Magnetoelectric coupling effects in multiferroic complex oxide composite structures. Adv Mater 22:2900–2918. https://doi.org/10.1002/adma.200904326.

[14] Rabe KM, Ahn CH, Triscone JM (2007) Physics of Ferroelectrics: A Modern Perspective. Springer, Berlin.

[15] Katsufuji T, Masaki M, Machida A, Moritomo M, Kato K, Nishibori E, Takata M, Sakata M, Ohoyama K, Kitazawa K, Takag H (2002) Crystal structure and magnetic properties of hexagonal $RMnO_3$ (R = Y, Lu, and Sc) and the effect of doping.Phys Rev B 66:134434. https://doi.org/10.1103/PhysRevB.66.134434.

[16] Prellier W, Singh MP, Murugavel P (2005) The single-phase multiferroic oxides: from bulk to thin film. J Phys-Condens Mat 17 R803–R832. https://doi.org/10.1088/0953-8984/17/30/R01.

[17] Fiebig M, Degenhardt C, Pisarev RV (2002) Magnetic phase diagram of $HoMnO_3$. J Appl Phys 91:8867–8869. https://doi.org/10.1063/1.1450837.

[18] Toulouse C, Liu J, Gallais Y, Measson MA, Sacuto A, Cazayou M, Chaix L, Simonet V, de Brion S, Pinsard-Godart L, Willaert F, Brubach JB, Roy P, Petit S (2014) Lattice and spin excitations in multiferroic h-$YMnO_3$. Phys Rev B 89:094415. https://doi.org/10.1103/PhysRevB.89.094415.

[19] Harikrishnan S, Rößler S, Naveen Kumar CM, Bhat HL, Rößler UK, Wirth S, Steglich F, Elizabeth S (2009) Phase transitions and rare-earth magnetism in hexagonal and orthorhombic $DyMnO_3$ single crystals. J Phys Condens Matter 21:096002–096012. https://doi.org/10.1088/0953-8984/21/9/096002.

[20] Sharma N, Das A, Prajapat CL, Singh MR (2016) Effect of rare earth dopants on the magnetic ordering of frustrated h-$YMnO_3$. J Magn Magn Mater 420:249–257. https://doi.org/10.1016/j.jmmm.2016.07.043.

[21] Tomczyk M, Senos AM, Vilarinho PM, Reaney IM (2012) Origin of microcracking in $YMnO_3$ ceramics. Scripta Mater 66:288–291. https://doi.org/10.1016/j.scriptamat.2011.11.014.

[22] Han TC, Wu PJ, Shih YL (2012) Correlation between magnetic ordering and electric polarization in $YMn_{1-x}Fe_xO_3$ nanocrystalline materials. J Appl Phys 111:07B511. http://link.aip.org/link/doi/10.1063/1.3673412.

[23] Ma Y, Chen XM, Wu YJ, Lin YQ (2010) Dielectric relaxation and enhanced multiferroic properties in $YMn_{0.8}Fe_{0.2}O_3$ ceramics prepared by in situ spark plasma sintering. Ceram Int 36:727–731. https://doi.org/10.1016/j.ceramint.2009.11.002.

[24] Wan F, Bai X, Song K, Lin X, Han X, Zheng J, Cao C (2017) Structure and magnetism of Cr-doped h-$YMnO_3$. J Magn Magn Mater 424:371. http://dx.doi.org/10.1016/j.jmmm.2016.10.088.

[25] Zhang AM, Zhu WH, Wu XS, Qing B (2011) Effect of Al doping on the microstructure properties of $YMn_{1-x}Al_xO_3$. J Cryst Growth 318:912–915. https://doi.org/10.1016/j.jcrysgro.2010.10.182.

[26] Amrani ME, Ta Phuoc V, Ammar MR, Zaghrioui M, Gervais F (2012) Structural modifications of disordered $YMn_{1-x}In_xO_3$ solid solutions evidenced by infrared and Raman spectroscopies. Solid State Sci 14:1315. http://dx.doi.org/10.1016/j.solidstatesciences.2012.06.013.

[27] Tian W, Tan G, Liu L, Zhang J, Winn B, Hong T, Fernandez-Baca JA, Zhang C, Dai P (2014) Influence of doping on the spin dynamics and magnetoelectric effect in hexagonal $Y_{0.7}Lu_{0.3}MnO_3$. Phys Rev B 89:144417. http://dx.doi.org/10.1103/PhysRevB.89.144417

[28] Moreno Botello ZL, Montenegro A, Grimaldos Osorio N, Huvé M, Pirovano C, Smabraten DR, Selbach SM, Caneiro A, Roussel P, Gauthier GH (2019) Pure and Zr-doped $YMnO_{3+\delta}$ as a YSZ-compatible SOFC cathode: a combined computational and experimental approach. J Mater Chem A 7:18589. https://doi.org/10.1039/C9TA04912F.

[29] Karoblis D, Zarkov A, Garskaite E, Mazeika K, Baltrunas D, Niaura G, Beganskiene A, Kareiva A (2021) Study of gadolinium substitution effects in hexagonal yttrium manganite $YMnO_3$. Sci Rep 11:2875. https://doi.org/10.1038/s41598-021-82621-6.

[30] Li SZ, Wang TT, Han HQ, Wang XZ, Li H, Liu J-M (2012) Modulated multiferroicity of Cr-doped orthorhombic polycrystalline $YMnO_3$. J Phys D Appl Phys 45:055003–055010. http://dx.doi.org/10.1088/0022-3727/45/5/055003.

[31] Shannon RD (1976) Revised effective ionic radii and systematic studies of interatomic distances in halides and chalcogenides. Acta Cryst A32:751–767. https://doi.org/10.1107/S0567739476001551.

[32] Levin I, Krayzman V, Vanderah TA, Tomczyk M, Wu H, Tucker MG, Playford HY, Woicik JC, Dennis CL, Vilarinho PM (2017) Oxygen-storage behavior and local structure in Ti-substituted $YMnO_3$. J Solid State Chem 246:29–41. https://doi.org/10.1016/j.jssc.2016.10.029.

[33] Okunaka S, Tokudome H, Hitomi Y, Abe R (2015) Facile preparation of stable aqueous titania sols for fabrication of highly active TiO_2 photocatalyst films. J Mater Chem A 3:1688-1695. https://doi.org/10.1039/C4TA04680C.

[34] Kraus W, Nolze G, PowderCell for Windows, V.2.4, Federal Institute for Materials Research and Testing, Berlin, Germany.

[35] Garwey RG, LSUCRIPC, least squares unit-cell refinement with indexing on the personal computer, Powder Diffr. 1 (1986) 114-118. doi:10.1017/S0885715600011465.

[36] Rodriguez-Carvajal J, FULLPROF: A program for Rietveld refinement and pattern matching analysis, Version 1.9c, France, 2001.

[37] Roisnel T, Rodriguez-Carvajal J, WINPLOTR: A graphic tool for powder diffraction, France, 2005. http://www-llb.cea.fr/fullweb/winplotr/winplotr.htm.

[38] Asaka T, Nemoto K, Kimoto K, Arima T, Matsui Y (2005) Crystallographic superstructure of Ti-doped hexagonal $YMnO_3$. Phys Rev B 71:014114. https://doi.org/10.1103/PhysRevB.71.014114.

[39] Wang M, Wang T, Song S, Ravi M, Liu R, Ji S (2017) Enhanced multiferroic properties of $YMnO_3$ ceramics fabricated by spark plasma sintering along with low-temperature solid-state reaction. Materials 10:474. https://doi.org/10.3390/ma10050474.

[40] Liu SH, Huang JCA, Qi X, Lin WJ, Siao YJ, Lin CR, Chen JM, Tang MT, Lee YH, Lee JC (2011) Structural transformation and charge transfer induced

ferroelectricity and magnetism in annealed $YMnO_3$. AIP Adv 1:032173. http://doi/10.1063/1.3647519.

[41] Wang M, Wang T, Song S, Ravi M, Liu R, Ji S (2017) Enhanced Multiferroic Properties of $YMnO_3$ Ceramics Fabricated by Spark Plasma Sintering Along with Low-Temperature Solid-State Reaction. Materials 10:474. doi:10.3390/ma10050474.

[42] Choi T, Horibe Y, Yi HT, Choi YJ, Wu W, Cheong SW (2010) Insulating interlocked ferroelectric and structural antiphase domain walls in multiferroic $YMnO_3$. Nat Mater 9:253. DOI: 10.1038/nmat2632.

[43] Lima AF, Lalic MV (2016) Ground-state magnetic structure of hexagonal $YMnO_3$ compound: A non-collinear spin density functional theory study. J Magn Magn Mater 416:236–240. https://doi.org/10.1016/j.jmmm.2016.05.038.

[44] Reehuis M, Tovar M, Tobbens DM, Pattison P, Hoser A, Lake B (2015) Competing Jahn-Teller distortions and ferrimagnetic ordering in the geometrically frustrated system $Ni_{1-x}Cu_xCr_2O_4$. Phys Rev B 91:024407. https://doi.org/10.1103/PhysRevB.91.024407.

[45] Park J, Kang M, Kim J, Lee S, Jang KH, Pirogov A, Park JG, Lee C, Park SH, Kim HC (2009) Doping effects of multiferroic manganites $YMn_{0.9}X_{0.1}O_3$ (X = Al, Ru, and Zn). Phys Rev B 79:064417. https://doi.org/10.1103/PhysRevB.79.064417.

[46] Zorko A, Pregelj M, Gomilšek M, Jagličić Z, Pajić D, Telling M, Arčon I, Mikulska I, Valant M (2015) Strain-induced extrinsic high-temperature ferromagnetism in the Fe-doped hexagonal barium titanate. Sci Rep UK 5:7703. https://doi.org/10.1038/srep07703.